

Nanoscale

Accepted Manuscript



This is an *Accepted Manuscript*, which has been through the Royal Society of Chemistry peer review process and has been accepted for publication.

Accepted Manuscripts are published online shortly after acceptance, before technical editing, formatting and proof reading. Using this free service, authors can make their results available to the community, in citable form, before we publish the edited article. We will replace this *Accepted Manuscript* with the edited and formatted *Advance Article* as soon as it is available.

You can find more information about *Accepted Manuscripts* in the [Information for Authors](#).

Please note that technical editing may introduce minor changes to the text and/or graphics, which may alter content. The journal's standard [Terms & Conditions](#) and the [Ethical guidelines](#) still apply. In no event shall the Royal Society of Chemistry be held responsible for any errors or omissions in this *Accepted Manuscript* or any consequences arising from the use of any information it contains.

Improved Performance of SrFe₁₂O₁₉ Bulk Magnets through Bottom-Up Nanostructuring

Matilde Saura-Múzquiz,¹ Cecilia Granados-Miralles,¹ Marian Stingaciu,¹ Espen Drath Bøjesen,¹ Qiang Li,² Jie Song,² Mingdong Dong,² Espen Eikeland¹ and Mogens Christensen^{1*}

¹ Center for Materials Crystallography, Department of Chemistry and Interdisciplinary Nanoscience Center (iNANO), Aarhus University, Langelandsgade 140, 8000 Aarhus C, Denmark

² Center for Nanotechnology (CDNA), Interdisciplinary Nanoscience Center (iNANO), Aarhus University, Gustav Wieds Vej 14, 8000 Aarhus C Denmark

*e-mail address of corresponding author: mch@chem.au.dk

Abstract

The influence of synthesis and compaction parameters is investigated with regards to formation of high performance SrFe₁₂O₁₉ bulk magnets. The produced magnets consist of highly aligned, single-magnetic domain nanoplatelets of SrFe₁₂O₁₉. The relationship between the magnetic performance of the samples and their structural features is established through systematic characterization by Vibrating Sample Magnetometry (VSM) and Rietveld refinement of powder X-ray diffraction data (PXRD). The analysis is supported by complementary techniques including Transmission Electron Microscopy (TEM), Atomic Force Microscopy (AFM) and X-ray pole figure measurements. SrFe₁₂O₁₉ hexagonal nanoplatelets with various sizes are synthesized by a supercritical hydrothermal flow method. The crystallite sizes are tuned by varying the Fe/Sr ratio in the precursor solution. Compaction of SrFe₁₂O₁₉ nanoplatelets into bulk magnets is performed by Spark Plasma Sintering (SPS). Rietveld refinement of the pressed pellets and texture analysis of pole figure measurements reveal that SPS pressing produces a high degree of alignment of the nanoplatelets, achieved without applying any magnetic field prior or during compaction. The highly aligned nanocrystallites combined with crystal growth during SPS give rise to an enormous enhancement of the magnetic properties compared to the as-synthesized powders, leading to high performance bulk magnets with energy products of 26 kJ m⁻³.

Keywords

Magnetism, strontium hexaferrite, hydrothermal synthesis, nanoplatelets, texture

Introduction

Magnetic materials are of key importance in a large variety of scientific and technological applications such as data storage,^{1, 2} biomedicine,^{3, 4} and electric motors.⁵ Since the discovery of high performance rare-earth magnets, conventional ferrite magnets have attracted less attention. However, recent geopolitical circumstances have sparked the need for new and cheaper magnetic materials with reduced content or even free of rare-earth elements.^{6, 7}

Nano-structuring of conventional magnetic ferrites has the potential to significantly improve their magnetic performance making them a viable alternative for certain applications.^{8, 9} An excellent candidate is the hexaferrite $\text{SrFe}_{12}\text{O}_{19}$ due to its pronounced magnetocrystalline anisotropy.¹⁰ The magnetic performance of $\text{SrFe}_{12}\text{O}_{19}$ has not been significantly improved within the last 20 years.¹¹ Nonetheless, a substantial enhancement may be achieved by controlling the material structure from the atomic to the microscopic scale. By matching the crystallite size of magnetic compounds to the magnetic domain size, it is possible to increase the coercivity and thereby maximize the energy product. This size matching has successfully been achieved by jet milling for $\text{Nd}_2\text{Fe}_{14}\text{B}_3$.¹² However, attempts to reduce the size of hexaferrites through ball milling have so far been unsuccessful, as it gives rise to partial phase transformation into $\alpha\text{-Fe}_2\text{O}_3$, Fe_3O_4 and an amorphous phase.¹³⁻¹⁶

Alternatively, the hydrothermal method is a cheap and energy efficient way of synthesizing hexaferrite nanocrystallites by a bottom-up approach, as demonstrated by Hakuta *et al.* in 1998 for the synthesis of $\text{BaFe}_{12}\text{O}_{19}$.¹⁷ This ferrite is one of the most extensively manufactured permanent magnetic materials. However, Ba^{2+} ions and barium-soluble compounds are toxic to humans, causing symptoms like hypertension, muscle weakness and paralysis.¹⁸ An alternative to the use of barium is the substitution by strontium, to form $\text{SrFe}_{12}\text{O}_{19}$, which has a comparable magnetic performance. However, to the best of our knowledge no report in literature describes the supercritical flow synthesis of $\text{SrFe}_{12}\text{O}_{19}$.

A number of studies on the hydrothermal synthesis of $\text{SrFe}_{12}\text{O}_{19}$ have been performed, in which the influence of various synthesis parameters is analyzed e.g., the $\text{OH}^-/\text{NO}_3^-$ ratio,¹⁹ the Sr/Fe ratio,^{19, 20} the reaction temperature,^{21, 22} etc. Unfortunately, this synthesis is not trivial and in most cases SrCO_3 and $\alpha\text{-Fe}_2\text{O}_3$ as well as other impurities are obtained along with the hexaferrite. In case of $\text{SrFe}_{12}\text{O}_{19}$, unlike the hydrothermal synthesis of $\text{BaFe}_{12}\text{O}_{19}$,²³ it is necessary to use a large excess of Sr in order to form the pure phase. Furthermore, high temperatures, long reaction times or subsequent annealing treatments are required to obtain a pure product, further complicating the formation of nanosized crystallites.

In the present study, the aim is to enhance the magnetic properties of $\text{SrFe}_{12}\text{O}_{19}$ through a bottom-up synthesis approach. In order to do so, single domain $\text{SrFe}_{12}\text{O}_{19}$ nanocrystallites were synthesized by supercritical flow synthesis. Hexagonal nanoplatelets of various sizes and aspect ratios were obtained by varying the Fe/Sr ratio in the precursor solution. Compaction of the tailored nanoplatelets into magnetically aligned bulk magnets was performed using Spark Plasma Sintering (SPS). The influence of SPS on texture, crystallite size and morphology was analyzed. Subsequently, the measured magnetic properties of the as-synthesized nanocrystallites and their corresponding compacted pellets were compared. With this work it is demonstrated how structural control through synthesis and compaction allows for control of the magnetic performance of the products, leading to magnetically aligned $\text{SrFe}_{12}\text{O}_{19}$ bulk magnets with a high energy product of 26 kJ m^{-3} .

Experimental Section

Synthesis and compaction

Precursor Preparation

Iron and strontium nitrates ($\text{Fe}(\text{NO}_3)_3 \cdot 9\text{H}_2\text{O}$ and $\text{Sr}(\text{NO}_3)_2$) technical grade (purity $\geq 98\%$ and $\geq 99\%$ respectively, Sigma-Aldrich) were dissolved in deionized water to obtain the precursor solutions with varying Fe/Sr ratios. The final concentration of $\text{Fe}(\text{NO}_3)_3 \cdot 9\text{H}_2\text{O}$ was 0.05 M in all cases, and the $\text{Sr}(\text{NO}_3)_2$ concentration was varied accordingly, to obtain three different Fe/Sr ratios equal to 1/1, 2/1 and 4/1. NaOH was added drop wise under constant magnetic stirring, in twice the molar amount of the nitrates, resulting in a dark red precipitate.

Supercritical Flow Reactor

The synthesis was carried out using a supercritical flow reactor; the detailed description of the setup was published by Mi *et al.*²⁴ The precursor solutions were pumped into the supercritical flow reactor at a flow rate of 5 mL/min. Deionized water was fed from a second line at a flow rate of 15 mL/min, and heated above the supercritical temperature passing through a pre-heater set to 300 °C and a main solvent heater set to 390 °C. The temperature of the main reactor was 390 °C and the system was pressurized to 250 bar. The collected products were centrifuged, washed with dilute HNO_3 2M, water and ethanol, and dried in air. The HNO_3 washing removes carbonates present in the as-synthesized products. Three powder samples were obtained from the three precursor solutions with different Fe/Sr ratios (1/1, 2/1 and 4/1), named FLOW-1, FLOW-2 and FLOW-4, respectively.

Spark Plasma Sintering (SPS)

Compaction of the as-synthesized nanoparticles into bulk magnets was performed under vacuum on a SPS Syntex Inc. 1500 model, Dr. Sinter LabTM series Spark Plasma Sintering system. The sintering technique is based on passing a pulsed DC current through a graphite die containing the powders, while a uniaxial pressure is applied.

The pressed pellets were polished to remove the layer of protecting graphite paper, obtaining smoothed-surface $\text{SrFe}_{12}\text{O}_{19}$ pellets of 8 mm diameter and ~1 mm thickness. Approximately 0.3 g of hydrothermally synthesized nanocrystallites were employed for the production of each pellet. A maximum pressure of 80 MPa and temperature of 950 °C were applied for 2 minutes to the three hydrothermally synthesized powder samples FLOW-1, FLOW-2 and FLOW-4, forming the corresponding SPS pellets, named SPS-1, SPS-2 and SPS-4, respectively. The density of the pressed pellets was obtained from their dimensions and weight, and was found to be slightly higher than 80%.

Annealing

The SPS-1 sample was cut in six pieces with approximate dimensions of $2 \times 2 \times 1 \text{ mm}^3$ to study the influence of post-SPS annealing on the magnetic properties. Each piece of the pellet was annealed for different times (2 h, 4 h, 8 h, 16 h and 24 h) at 850 °C in a high temperature furnace (GERO Hochtemperaturöfen GmbH D-75242 Neuhausen), and subsequently quenched in air.

Characterization

Powder X-ray Diffraction

Diffraction patterns of the hydrothermally synthesized samples were collected on a Rigaku SmartLab diffractometer (Rigaku, Japan) using Cu radiation. Cross Beam Optics and a Ge(220)x2 double bounce monochromator were used to obtain Cu $K_{\alpha 1}$ radiation. The diffracted beam was collected with a Dtex/Ultra detector set to fluorescence suppression mode. Powder diffraction patterns collected on the as-obtained SPS pellets were measured using a Rigaku SmartLab diffractometer (Rigaku, Japan), with Cu $K_{\alpha 1,2}$ radiation with parallel beam incident optics, and a Dtex/Ultra detector set to fluorescence suppression mode. The pellet was mounted with the flat surface perpendicular to the scattering vector. A NIST LaB₆ 660b standard was measured on the Rigaku SmartLab diffractometer in the same conditions as the corresponding samples for determination of instrumental broadening.

Portions of the SPS pellets were crushed into powders and packed into 0.4 mm diameter capillaries. High resolution X-ray powder diffraction patterns were collected at beamline BL44B2,²⁵ SPring-8 synchrotron, Harima Science Park, Hyogo Prefecture, Japan, using a wavelength of 0.5 Å. The measurement of a NIST CeO₂ was carried out for determination of instrumental broadening.

All powder X-ray diffraction patterns were analyzed by Rietveld refinement using the *Fullprof Suite* software package.²⁶ The background was described using a Chebyshev polynomial function, while the peak profile was modeled using the Thompson-Cox-Hasting formulation of the pseudo-Voigt²⁷ function. Details on the Rietveld refinements can be found in Supporting Information.

Transmission Electron Microscopy

Micrographs of the hydrothermally synthesized products were collected using a Phillips CM20 200 kV TEM. For sample preparation, a small portion of the nanocrystallites was suspended in ethanol and sonicated for 30 minutes.

Atomic Force Microscopy

AFM measurements of the hydrothermally synthesized nanocrystallites were performed with a commercial AFM MultiMode V (Bruker, Santa Barbara, USA). A small portion of the as-synthesized nanocrystallites was dispersed into ethanol and sonicated for 5 mins. Subsequently, 5 μ L of the dispersion were dropped onto a Mica substrate. Once the ethanol had evaporated, the sample was characterized by AFM directly in tapping mode with ultrasharp silicon cantilevers (OMCL-AC160TS-R3; Olympus).

Vibrating Sample Magnetometry (VSM)

Hysteresis loops were measured with a Quantum Design Physical Property Measurement System (PPMS) equipped with a Vibrating Sample Magnetometer (VSM). The field dependent magnetization was measured at room temperature, by scanning the external field between ± 1.5 T. The powder samples were cold pressed into 3 mm diameter and ~ 1 mm thick pellets to prevent physical movement of the nanocrystallites during the measurement. In the case of the SPS samples, a fragment of the pellet was cut with approximate dimensions of $2 \times 2 \times 1$ mm³, and fixed in place with the flat surface of the pellet perpendicular to the applied field. All the data were treated considering a weighted-average density, obtained by the refined weighted fractions and densities of the different phases present in each sample.

The considered saturation magnetization value, M_s , corresponds in all cases to the magnetization value at the applied field of 1.5 T. The effective field, H_{eff} , is the corrected applied field, *i.e.* $H_{\text{eff}} = H_{\text{app}} - NM$. In the case of polycrystalline samples, the demagnetizing factor N is dependent on the shape of the crystallites, as well as the shape of the macroscopic sample, the packing fraction and the degree of crystallite orientation. In order to make the magnetic results more comparable between the different samples, the approximation of a demagnetizing factor N of 0.33, corresponding to isotropic particles, was used for all samples. As an alternative to this approximation, an experimental calculation of N could be performed graphically for each of the SPS samples given the squareness of their hysteresis loops. Doing so, sample SPS-1 would have an N value equal of 0.63, which gives rise to a BH_{max} of 28 kJ m^{-3} . See Supporting Information for further explanation and details on the experimental calculation of N .

Results

Tailor-made $\text{SrFe}_{12}\text{O}_{19}$ nanoplatelets were synthesized by the supercritical hydrothermal method in the continuous flow reactor. Three different samples were obtained from precursors with different Fe/Sr ratios equal to 1/1, 2/1 and 4/1, named FLOW-1, FLOW-2 and FLOW-4, respectively. The three as-synthesized samples were compacted by SPS to form three bulk magnets of aligned nanocrystallites, denoted SPS-1, SPS-2 and SPS-4 respectively. In order to understand and define the magnetic performance of the produced $\text{SrFe}_{12}\text{O}_{19}$ magnets, a thorough characterization and analysis of each step of the process was performed.

Powder Samples (as-synthesized nanocrystallites)

X-ray Diffraction: Rietveld Refinements

Anisotropic $\text{SrFe}_{12}\text{O}_{19}$ nanocrystallites: X-ray powder diffraction of the as-synthesized nanocrystallites reveals the majority phase to be $\text{SrFe}_{12}\text{O}_{19}$, see Figure 1 (a). Pronounced differences in relative peak broadening and relative intensities within each diffraction pattern are readily observed, especially for sample FLOW-1. This is an indication of the highly anisotropic shape of the nanoplatelets. The sharp peaks for (110) and (220) reflections indicate large sizes along the a - and b -axes, while the broad peaks for (00 l) reflections imply thin crystallites with respect to the c -axis. The unit cell structure of the $\text{SrFe}_{12}\text{O}_{19}$ phase is shown in Figure 1 (b), and a hexagonal platelet illustrating the anisotropic crystallite morphology is shown in Figure 1 (c). For FLOW-1 and FLOW-2 the initial single-phase $\text{SrFe}_{12}\text{O}_{19}$ Rietveld model proved inadequate to describe the complex peak shape. Therefore an additional $\text{SrFe}_{12}\text{O}_{19}$ phase was implemented, resulting in a bimodal nanocrystallite size distribution. The lesser abundant of the two $\text{SrFe}_{12}\text{O}_{19}$ phases is, in both samples, the one with larger crystallite sizes, referred to as $\text{SrFe}_{12}\text{O}_{19}$ -II. This phase constitutes around 20 weight% in FLOW-2 and 3 weight% in FLOW-1. Given its predominance, only the most abundant phase ($\text{SrFe}_{12}\text{O}_{19}$ -I) was considered in the analysis and comparison of the crystallite sizes with varying Fe/Sr ratio. However, details on the bimodal refinement and the refined values of crystallite size for both, $\text{SrFe}_{12}\text{O}_{19}$ -I and $\text{SrFe}_{12}\text{O}_{19}$ -II are placed in Supporting Information. Figure 2 (a) shows the refined crystallite size along the a - and c -axis as a function of Fe/Sr ratio. A definite correlation between the iron content and crystallite size of $\text{SrFe}_{12}\text{O}_{19}$ can be established; increasing the Fe content leads to larger crystallites. Comparable crystallite sizes are observed for FLOW-1 and FLOW-2 with a diameter of 30.2(4) and 29.7(5) nm, and a thickness of 2.66(3) and 2.67(6) nm

respectively. However, the crystallite size is considerably larger for FLOW-4, where platelets of 80(1) nm in diameter and 27.3(3) nm in thickness are obtained. These changes in crystallite sizes result in decreasing a/c size ratio of the nanoplatelets with increasing Fe/Sr ratio. The obtained values for crystallite size and a/c aspect ratio are given in Table 1. The thickness of FLOW-1 and FLOW-2 platelets is extremely thin, almost identical to the unit cell value along the c -axis (2.309 nm).

Impurity phase: A careful inspection of the Rietveld refinements revealed the presence of an impurity phase in all samples. This secondary phase was identified and refined as the defect-free ferrihydrate structure (FeOOH) described by Jensen *et al.*,²⁸ in the space group $P\bar{3}1c$. In Figure 1 (a), the magnification of a selected 2θ region of sample FLOW-4 illustrates the presence of FeOOH. The unit cell of the structure is shown in Figure 1 (b). This phase also forms crystallites in the shape of platelets according to the Rietveld refinements. A schematic representation of a FeOOH crystallite is presented in Figure 1 (c). The content of FeOOH is dependent on the Fe/Sr ratio; see Figure 2 (b). Increasing the Fe/Sr ratio causes an increase of FeOOH from 11 weight% in FLOW-1, to 14 weight% in FLOW-2, to 51 weight% in FLOW-4. FeOOH crystallite sizes extracted from refinements are given in Table 1. Further information about the FeOOH phase can be found in Supporting Information.

In order to confirm the robustness of the X-ray diffraction analysis, complementary microscopy techniques were employed.

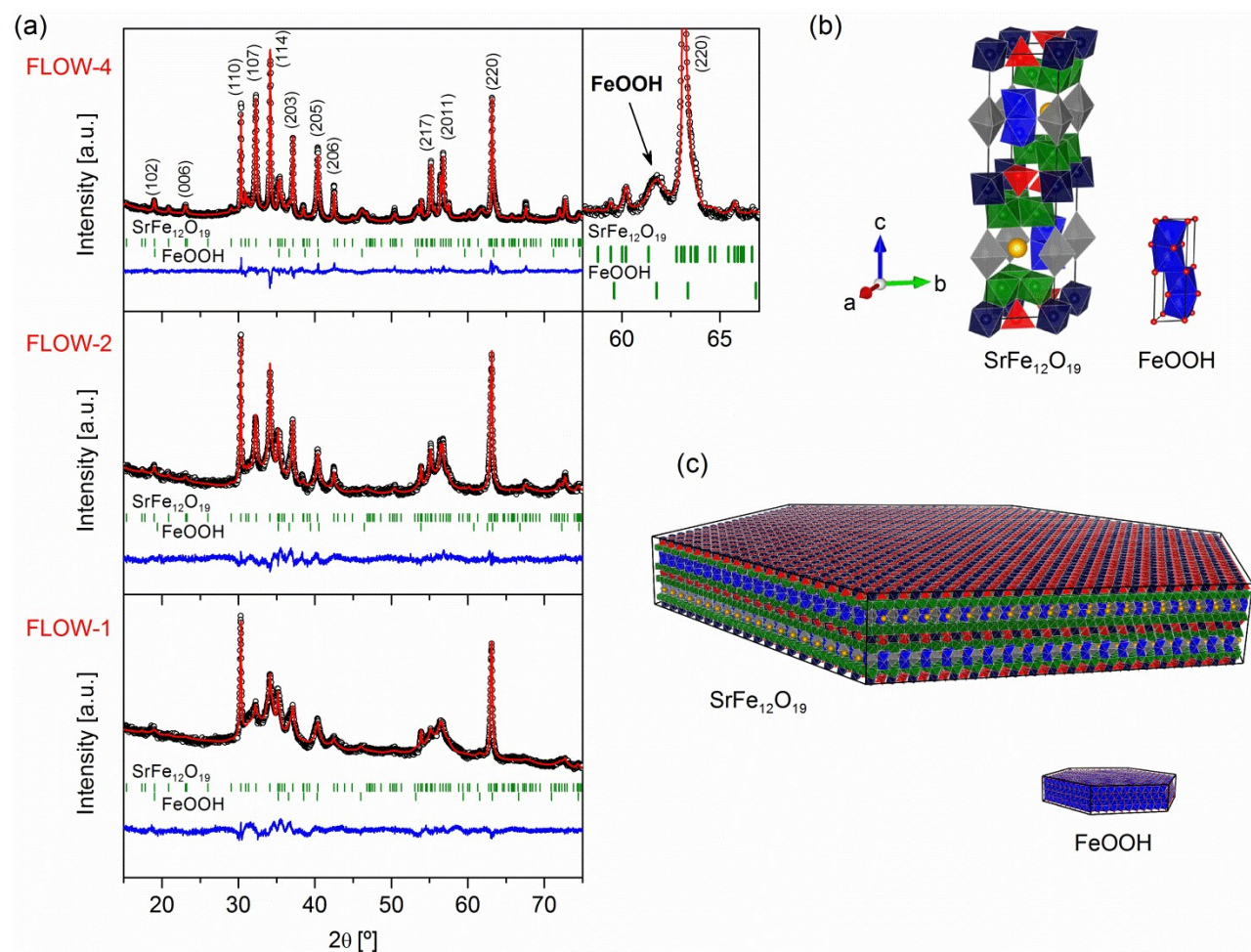


Figure 1: (a) Rietveld refinement of powder X-ray diffraction data of the three as-synthesized powder samples FLOW-1, FLOW-2 and FLOW-4. The black dots are the experimental data; the red line is the calculated Rietveld model; the positions of the Bragg peaks are represented with the green lines, and the blue line shows the difference between the observed and calculated intensities. (b) Representation of the atomic structure of one unit cell of $\text{SrFe}_{12}\text{O}_{19}$ and FeOOH , both performed with VESTA.²⁹ The differently colored polyhedra of $\text{SrFe}_{12}\text{O}_{19}$ represent the different crystallographic positions of the Fe^{3+} ions, and their coordination with the surrounding oxygen atoms. The yellow spheres represent the Sr atoms. (c) Schematic representation of hexagonal crystallites of $\text{SrFe}_{12}\text{O}_{19}$ and FeOOH performed with VESTA.

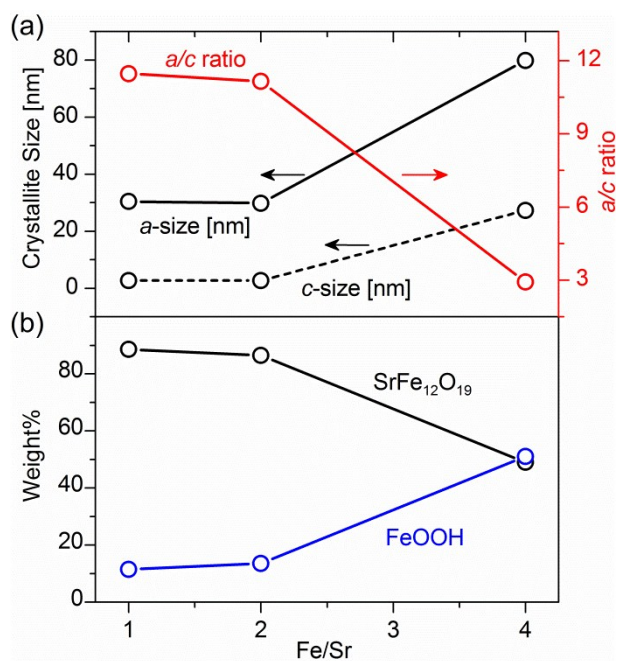


Figure 2: (a) Size and aspect ratio of $\text{SrFe}_{12}\text{O}_{19}$ crystallites for different Fe/Sr ratios. The error bars lie within the size of the circles. (b) Variation of phase composition with increasing Fe/Sr ratio.

Table 1: Phase composition and crystallite sizes extracted from the refinements of the three powder samples and the crushed SPS pellets (described in the X-ray diffraction subsection of section “SPS pellets (compacted nanocrystallites)”.

Sample	$\text{SrFe}_{12}\text{O}_{19}$ [Weight%]	$a=b^a$ [nm]	c^a [nm]	a/c	Secondary phase [Weight%]	$a=b$ [nm]	c [nm]
FLOW-1	89(1)	30.2(4)	2.66(3)	11.4	11(1) ^b	18(2)	6.4(6)
FLOW-2	86(2)	29.7(5)	2.67(6)	11.1	14(1) ^b	24(2)	3.6(2)
FLOW-4	49(1)	80(1)	27.3(3)	2.92	51(1) ^b	17.0(5)	5.1(1)
SPS-1	100.0(3)	102(2)	81(2)	1.26	<0.3 ^c	-	-
SPS-2	80.0(3)	109(2)	72(2)	1.51	20.0(2) ^c	95(2)	-
SPS-4	95.4(2)	81.6(8)	53.1(7)	1.54	4.6(1) ^d	88(4)	-

^a) Refined crystallite sizes of the main $\text{SrFe}_{12}\text{O}_{19}$ phase ($\text{SrFe}_{12}\text{O}_{19-1}$); ^b) FeOOH ; ^c) $\alpha\text{-Fe}_2\text{O}_3$; ^d) $\gamma\text{-Fe}_2\text{O}_3$

Microscopy: TEM and AFM

Transmission Electron Microscopy (TEM) and Atomic Force Microscopy (AFM) images were collected on all three powder samples. Representative TEM and AFM images of sample FLOW-1 are shown in Figure 3 (a). Both techniques confirm the platelet-like morphology and hexagonal symmetry of the nanocrystallites. In addition, particle sizes observed in TEM and AFM are comparable in magnitude to the crystallite sizes extracted from the diffraction data. This is interpreted as the platelets being single-crystalline. In the TEM micrograph of sample FLOW-1 the hexagonal platelets are observed to pile on top of each other forming “columns” of stacked nanoplatelets. This is most likely due to magnetic interactions between platelets; the easy axis of magnetization lies along the *c*-axis. Although some degree of stacking of platelets occurs in the other two samples, it is not as pronounced as in FLOW-1, where the platelets are smaller. TEM and AFM micrographs of sample FLOW-4 are shown in Figure 3 (b). In the micrographs large hexagonal platelets of sizes similar to those obtained from the refinement of sample FLOW-4 are observed. However, a large amount of smaller hexagonal platelets, with an approximate diameter of 20 nm, are also observed. These smaller platelets are most likely the FeOOH phase, which constitutes 51 weight% of the FLOW-4 sample. The observed particle size of these platelets on the TEM micrograph matches the refined crystallite size of FeOOH obtained from the diffraction data. The small platelets are not randomly dispersed through the sample, or forming agglomerates. They are on the surfaces of the larger SrFe₁₂O₁₉ platelets, possibly due to magnetic attraction.

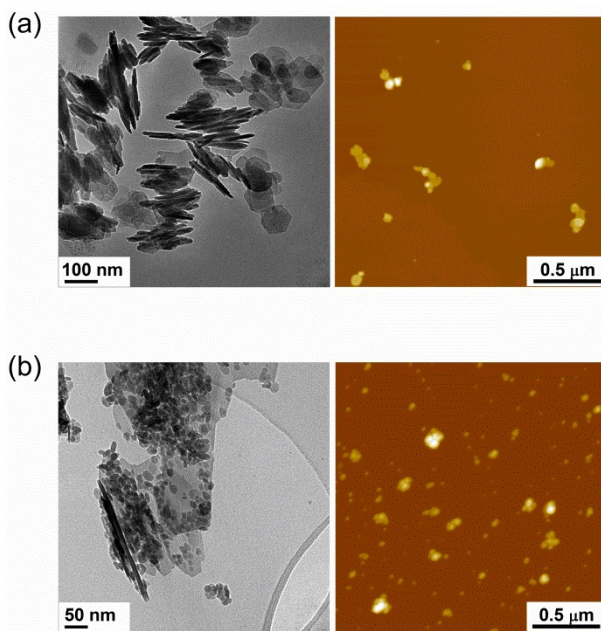


Figure 3: (a) TEM and AFM images of sample FLOW-1. Both, TEM and AFM confirm the hexagonal platelet morphology and crystallite size extracted from refinements. (b) TEM and AFM micrographs of sample FLOW-4. The morphology and crystallite size obtained from refinements is confirmed, as well as the existence of small platelet-like particles, which most likely correspond to the large amount of FeOOH present in that sample.

Magnetic Hysteresis at Room Temperature

The hysteresis curves (magnetization M vs. effective field H_{eff}) of the three hydrothermally synthesized samples are shown in Figure 4. The numeric values of the maximum energy product, BH_{max} , remanent magnetization, M_r , saturation magnetization, M_s , and coercive field, H_c , can be found in Table 2. The three curves have widely different shape; yet both FLOW-1 and FLOW-2 reach the same energy product.

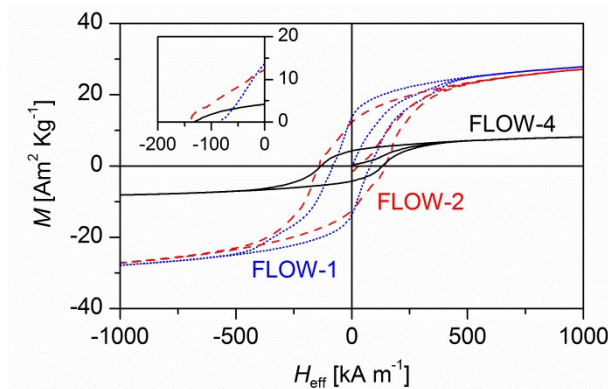


Figure 4: Magnetic hysteresis curves (Magnetization, M , vs. Effective Field, H_{eff}) of the three powder samples, and inset with magnification of the second quadrant of the hysteresis curves. FLOW-1 depicted in blue dots, FLOW-2 in red dashed lines, and FLOW-4 in solid black line.

Table 2: Numeric values of energy product (BH_{max}), remanent mass magnetization (M_r), saturation mass magnetization (M_s), M_r/M_s ratio and coercive field (H_c) of the three hydrothermally as-synthesized powder samples and their corresponding SPS pellets (described in the magnetic subsection of section “SPS PELLETS (compacted nanocrystallites)”.

Sample	BH_{max} [kJ m ⁻³]	M_r [Am ² Kg ⁻¹]	M_s [Am ² Kg ⁻¹]	M_r/M_s	H_c [kA m ⁻¹]	H_c [T]
FLOW-1	0.84	14	28	0.50	84	0.11
FLOW-2	0.84	12	28	0.43	139	0.17
FLOW-4	0.14	4	8	0.50	134	0.17
SPS-1	26	59	69	0.86	301	0.38
SPS-2	12	42	55	0.76	303	0.38
SPS-4	21	58	68	0.85	174	0.22

The remanent magnetization decreases with increasing iron content. M_r is slightly larger for FLOW-1 (14 Am² kg⁻¹) compared with FLOW-2 (12 Am² kg⁻¹), while FLOW-4 (4 Am² kg⁻¹) has the smallest observed remanence. The difference in M_r values between the three samples can be explained by the results obtained from the X-ray diffraction data. FLOW-4 was found to have the largest content of FeOOH (51 wt%) followed by FLOW-2 (14 wt%) and finally FLOW-1 (12 wt%), *i.e.*, increased FeOOH content will bring about lower M_r values. For all three samples the remanent magnetization to saturation magnetization ratio, M_r/M_s , is equal or close to 0.5, which is the theoretical M_r/M_s value for an assembly of randomly oriented single domain particles.³⁰

The coercive field is larger for FLOW-4 and FLOW-2 (134 kA m^{-1} and 139 kA m^{-1}), and smaller for FLOW-1 (84 kA m^{-1}). This is in agreement with the crystallite size increase. Larger crystallites give rise to higher coercive fields, as long as the critical diameter for multi-domain formation is not reached. Although FLOW-1 and FLOW-2 are mostly constituted by crystallites of equal size, FLOW-2 exhibits higher coercivity, due to the 20 weight% of larger $\text{SrFe}_{12}\text{O}_{19}$ crystallites ($\text{SrFe}_{12}\text{O}_{19}$ -II).

Despite the fact that the FLOW-4 contain 51 wt% FeOOH no kink in the hysteresis data is observed, this could be due to an effective exchange coupling between the ferromagnetic $\text{SrFe}_{12}\text{O}_{19}$ phase and the antiferromagnetic FeOOH .

SPS Pellets (compacted nanocrystallites)

X-ray Diffraction: Rietveld Refinements

Phase purity: Analysis of crystallite size and phase identification after SPS was carried out by crushing part of the pellets, measuring PXRD patterns and performing Rietveld refinement. The powder diffraction pattern of the crushed SPS samples were collected at beamline BL44B2 at SPring8²⁵. The Rietveld refined data for SPS-1 is shown in Figure 5. Rietveld refinements of the other two SPS samples and refined parameters can be found in Supporting Information.

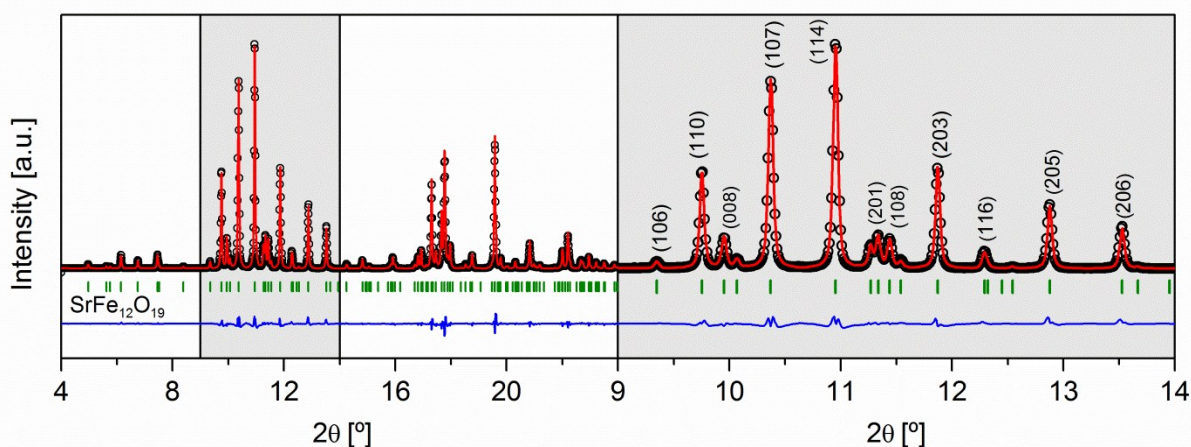
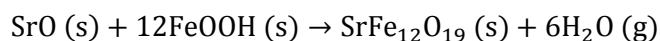


Figure 5: Rietveld refinement of the powder X-ray diffraction data from the crushed SPS-1 pellet, collected at SPring-8 synchrotron ($\lambda = 0.5000 \text{ \AA}$), and magnification of a 2θ region where the main peaks of the phase are indexed, and the high purity of the sample is observed. The black dots are the experimental data; the red line is the calculated Rietveld model; the positions of the Bragg peaks are represented with the green lines, and the blue line shows the difference between the observed and calculated intensities.

Results obtained from refinements reveal that the FeOOH phase, observed in the as-synthesized powders, is no longer present in any of the 3 samples after SPS. FeOOH appears to have been converted into $\text{SrFe}_{12}\text{O}_{19}$ during the compaction. This transformation implies the existence of strontium excess in the powder together with the hexaferrite. This strontium excess is likely present as SrO as large excess of strontium is used during the synthesis. However, no crystalline SrO is detected in any of the powder diffraction patterns recorded; suggesting that it is amorphous. The expected chemical reaction for the conversion of FeOOH is:



This reaction scheme is supported by a temporary breakage of the vacuum condition due to gas evolution during SPS. No impurity phases are readily detected in SPS-1 *i.e.* the impurity level is <0.3 weight%. However, 20 weight% of α -Fe₂O₃ is observed in SPS-2, while SPS-4 contains no α -Fe₂O₃, but 5 weight% of γ -Fe₂O₃ is present. The iron oxide phases could originate from partial transformation of the FeOOH phase due to insufficient local SrO concentration. The following reaction scheme is proposed:

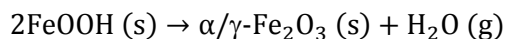


Table 1 gives the phase composition of the SPS samples, extracted from Rietveld refinements.

Crystallite growth: The pronounced peak sharpening in the powder diffraction data of the crushed SPS pellets compared with the as-synthesized samples indicates significant crystallite growth along both directions of the nanoplatelets during compaction. Crystallite sizes obtained from refinements of the three crushed SPS pellets are given in Table 1. The powder samples with small crystallites experience larger crystallite growth during SPS compared with the initial large crystallites. Furthermore, the crystallite growth is more pronounced along the *c*-axis compared to the *a*- and *b*-axes, giving rise to a change in the morphology of the nanoplatelets. The *a/c* ratio is much smaller for the compacted platelets compared to those of the as synthesized powders, and it increases with increasing Fe/Sr ratio.

Texture: To obtain information about the degree of alignment, powder X-ray diffraction patterns were collected on the as-obtained SPS pellets, with the pressing surface of the pellet perpendicular to the scattering plane. A comparison of the Rietveld refinement of the as-synthesized FLOW-1 powder sample and the corresponding SPS-1 pellet is shown in Figure 6 (a).

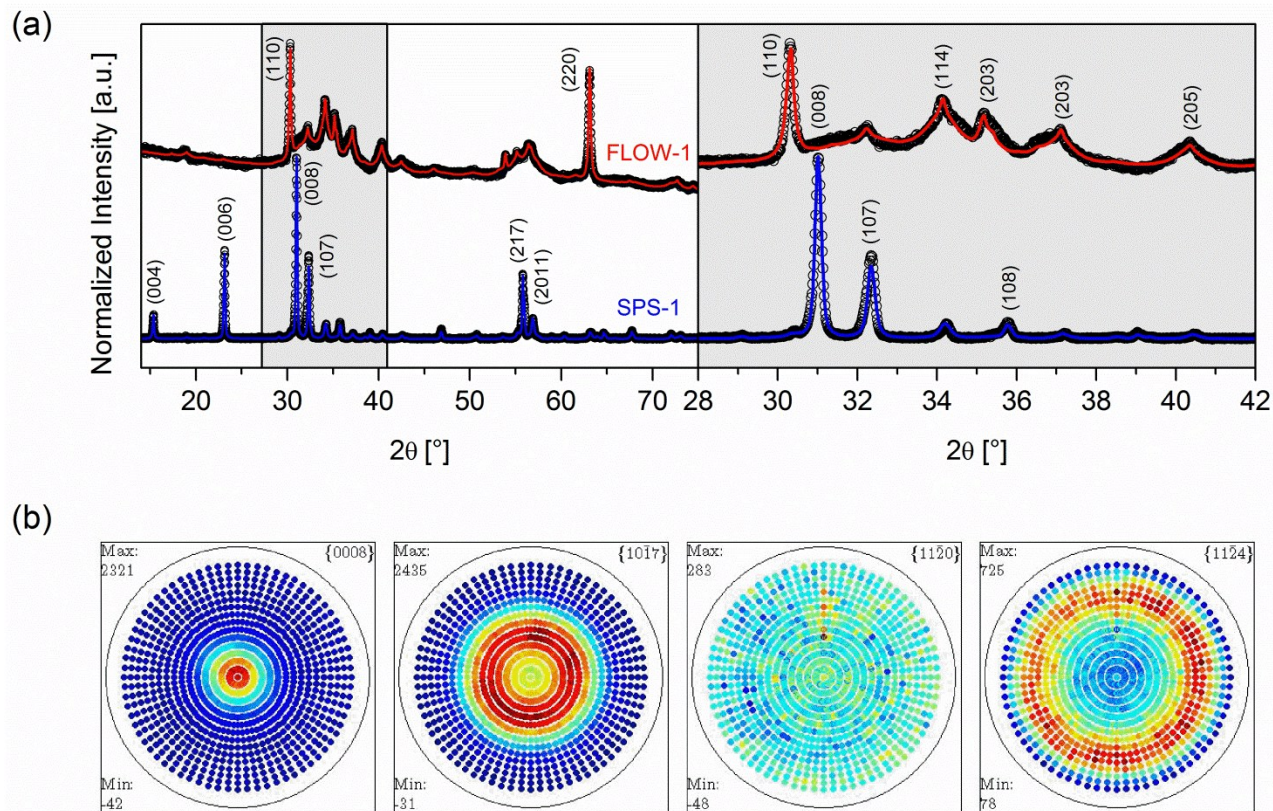


Figure 6: (a) Rietveld refinement of the as-synthesized nanoparticles FLOW-1 (refined in red) and their corresponding SPS pellet, SPS-1 (refined in blue). Magnification of the 2θ region marked with a grey rectangle is shown on the right hand side of the figure. The highly textured sample SPS-1 was modeled using the Modified March's function³¹ in *FullProf Suite*²⁶ to account for preferred orientation. (b) X-ray pole figure measurements of SPS-1 pellet. Measurements were performed in the full Φ range from 0° - 360° in steps of 5° , while χ was varied between 75° - 0° in steps of 5° .

From Figure 6 (a) it may appear as if a phase transformation has occurred during SPS. There is little resemblance between the two diffraction patterns. However, the change in the relative intensities of the peaks is an effect of a pronounced texture developing during the compaction. Diffraction peaks almost inexistent in FLOW-1 become the most intense peaks of SPS-1, and vice versa. Indexing of the data reveals that the intense peaks observed in SPS-1 are those of Miller hkl -index with significant l character, corresponding to the crystallographic c -axis. This induced texture takes place without the application of an external magnetic field. It is due to the platelet-like morphology of the hydrothermally synthesized $\text{SrFe}_{12}\text{O}_{19}$ nanocrystallites. Due to the magnetic interaction between the platelets, they tend to stack on top of each other as seen in the TEM image in Figure 3. However, these stacked units will rotate with respect to each other to reduce the magnetostatic energy. Under an applied uniaxial pressure, non-magnetic platelets would normally align with their large surface perpendicular to the applied force. In the case of magnetic platelets, the magnetostatic energy will compete with the applied force for maintaining the domain rotation of the stacked units. The heat applied during SPS overcomes the magnetic interactions and, as a consequence, the platelets align with the applied uniaxial pressure. The resulting pellets have directional dependent properties along the c -axis, similar to those of a single crystal.

To obtain quantitative information about the alignment of the nanoplatelets in the pressed pellet, pole figure measurements were performed for SPS-1. The (008), (107), (110) and (114) pole figures of SPS-1 are shown in Figure 6 (b). The sharp variation of intensity with χ (from the center and outwards), and symmetry of diffraction intensity along 360° in Φ (concentric circumference in the plane of the paper) confirms high alignment of nanoparticles along the c -axis. The orientation distribution function (ODF) was generated from five poles ((008), (107), (110), (114) and (203)) using MTEX software.^{32, 33} The relative volume orientation of the crystallites with respect to $00l$ axis with increasing θ angle (polar coordinates) was subsequently extracted and plotted in Figure 7. The steps in θ are made in such a way, that they present a constant integrated volume of a sphere, when going from the pole to the equator. The extracted data shows that within the volume irradiated by X-rays $\sim 50\%$ of the crystallites are oriented within 25° of the $00l$ direction, 80% are oriented within 45° , and practically 100% are oriented within 75° . This indicates a high degree of texture, where the platelets are not perfectly horizontal in the compacted pellet, but with a preferred tilt between 15° and 30° .

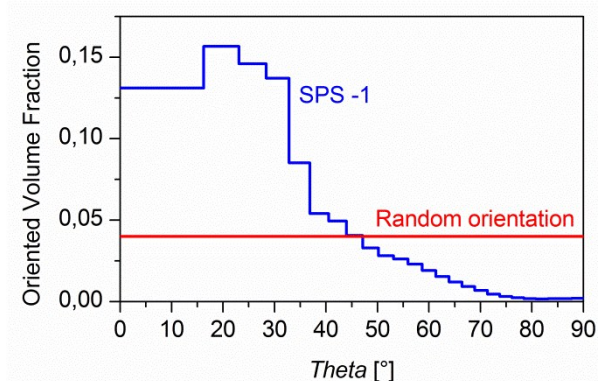


Figure 7: Oriented volume fraction of SPS-1 with increasing Θ angle obtained from the extracted ODF, and comparison with the value corresponding to a randomly oriented specimen.

Magnetic Hysteresis at Room Temperature

Compaction of the as-synthesized powders through SPS gives rise to a huge enhancement of the magnetic properties. Not only are the coercivity, saturation and remanent magnetization drastically enhanced; but also the hysteresis curves become highly rectangular, with M_r/M_s ratios of 0.76 – 0.86. Figure 8 (a) shows the hysteresis curve of SPS-1 (solid blue line) and of the as-synthesized powder FLOW-1 (dashed blue line). By comparison with the hysteresis of the as-synthesized powder, SPS causes the remanent magnetization to increase by more than 300%, and the coercivity by $\sim 250\%$. This results in an energy product 30 times larger than that of the corresponding powders. The two insets of Figure 8 (a) show the second quadrant of the hysteresis curves of the other two powder samples and their corresponding SPS pellets.

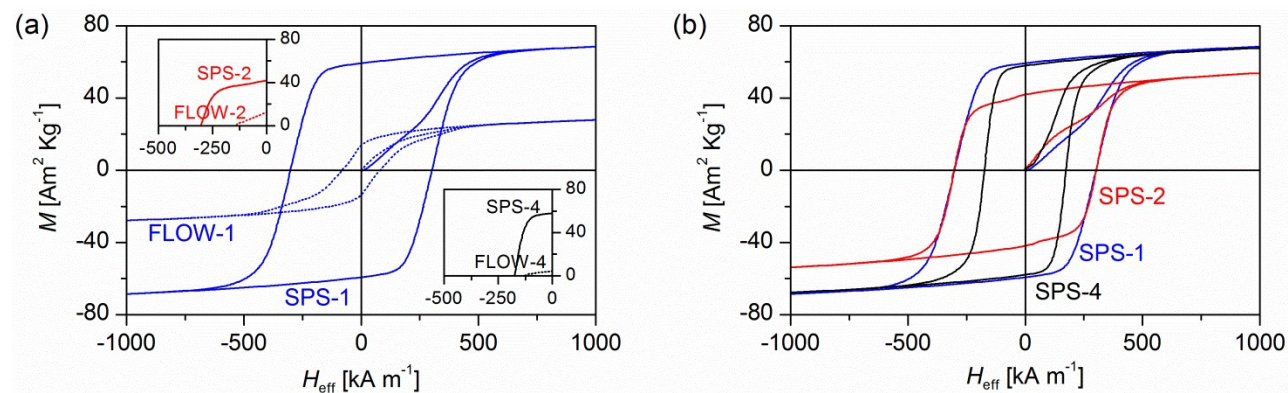


Figure 8: Magnetic hysteresis curves (Magnetization, M , vs. Effective Field, H_{eff}) of (a): powder samples and their corresponding SPS pellets and (b): comparison between the hysteresis curves of the three SPS pellets.

Comparison of the hysteresis curves from the three SPS samples is shown in Figure 8 (b), and numeric values of energy product, remanent magnetization, saturation magnetization, M_r/M_s ratio and coercivity are given in Table 2.

The knowledge obtained from X-ray diffraction analyses explains the differences in the hysteresis curves of Figure 8. The squareness of the hysteresis loops of the SPS pellets is a consequence of the highly oriented distribution of the nanoplatelets within the pellet. More than 80% of the maximum

magnetization is retained upon removal of the field in SPS-1 according to the hysteresis loop ($M_r/M_s = 0.86$). The 20% of the sample that does not retain the magnetization is in accordance with the ODF, where 20% corresponds to the volume of platelets with an angle larger than 45° between their *ab*-plane and the horizontal plane of the pellet.

The transformation of FeOOH into $\text{SrFe}_{12}\text{O}_{19}$ and $\gamma\text{-Fe}_2\text{O}_3$ during SPS explains the enhancement of the saturation and remanent magnetization of SPS-1 and SPS-4, while the large amount of hematite in SPS-2 diminishes the magnetization of this sample compared to the other two. The larger amount of impurity in SPS-2 also explains the “kink” in the hysteresis at around $\pm 90 \text{ kA m}^{-1}$, typically observed in multi-phased samples.

The increase in crystallite size is the direct origin of the enhanced coercivity of the SPS pellets with respect to the powders. Those containing the largest nanocrystallites have the largest coercive values suggesting that the crystallite growth of the initial powders caused by SPS has not yet reached the critical diameter for multi-domain formation. This is also in agreement with the calculations made by Zi *et al.* and Luo *et al.*, who estimated the maximum diameter for single domain particles of $\text{SrFe}_{12}\text{O}_{19}$ to be about 650 nm and 516 nm respectively.^{34, 35} Furthermore, the noticeable lower coercivity of SPS-4 with respect to the other two pellets is most likely caused by the presence of the magnetically soft $\gamma\text{-Fe}_3\text{O}_4$ phase, exclusively observed in this sample.

The large enhancement of magnetic properties after SPS gives rise to a maximum energy product of 26 kJ m^{-3} for SPS-1, due to its high purity and larger crystallite size compared to the other two samples. An energy product of 21 kJ m^{-3} is obtained by SPS-4, whereas a considerably lower value of 12 kJ m^{-3} is observed for SPS-2.

Post-SPS Annealing

The SPS pellet with the highest BH_{max} , SPS-1, was cut in smaller pieces of equal dimensions, which were annealed at 850°C for different times (2 h, 4 h, 8 h, 16 h and 24 h). Magnetic hysteresis curves were subsequently measured on the pieces of SPS-1 to study the influence of post-SPS annealing on the magnetic properties. The variation of energy product with increasing annealing time is shown in Figure 9. An improved energy product is attained when increasing the annealing time up to 4 hours, where the maximum energy product of 28.4 kJ m^{-3} is reached. Further increase in annealing time leads to a gradual decrease in the energy product to a value of 23.5 kJ m^{-3} after 24 hours of annealing; thus, attaining a lower value than the observed for the initial SPS-1 pellet. The detected 11% increase in BH_{max} after 4 hours of annealing suggests that the SPS compaction can still be optimized to reach larger energy products. The reasoning behind the observed trend in energy product with annealing time needs further investigation.

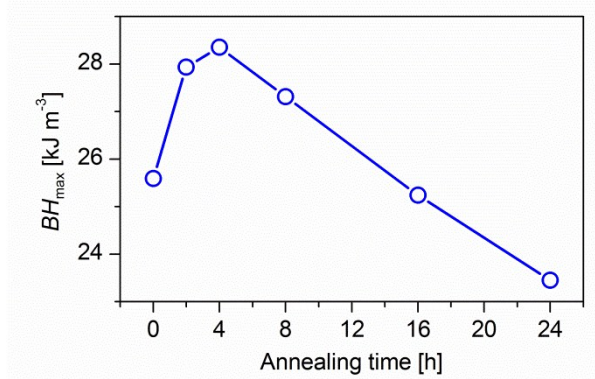


Figure 9: Variation of maximum energy product with post-SPS annealing at 850 °C and varying time for SPS-1.

Discussion

Hydrothermal syntheses of $\text{SrFe}_{12}\text{O}_{19}$ have previously been reported in literature. However, in the majority of studies only the size along the *ab*-plane of the platelets is reported, and is obtained exclusively from microscopy techniques.^{19-22, 36-39} Only a few studies on the strontium hexaferrite contain refinements of the powder diffraction data to obtain further information than phase identification by peak indexing.^{34, 40} However, these studies do not consider the anisotropic platelet-like shape of the crystallites in the refinements, and therefore report a single size obtained by modeling isotropic crystallites.

The presented study is, to the best of our knowledge, the first study employing platelet modeling of nanocrystallites by Rietveld analysis of powder diffraction patterns to investigate $\text{SrFe}_{12}\text{O}_{19}$ morphology. Furthermore, the presence of the ferrihydrate FeOOH phase can also be observed in the powder patterns from previously reported $\text{SrFe}_{12}\text{O}_{19}$ syntheses.⁴¹ However it is easily misinterpreted or ignored due to the pronounced broadening of the diffraction peaks. Darinka Primc *et al.* carried out electron diffraction on the FeOOH platelets and observed interplanar distances of ~ 0.95 nm in the *c*-axis, which match our refined value of the unit-cell *c*-axis of the FeOOH phase. Yet, their observation was interpreted as being ultrafine nanoparticles of $\text{SrFe}_{12}\text{O}_{19}$, despite the disagreement with the interplanar distances of $\text{SrFe}_{12}\text{O}_{19}$ along the *c*-axis.²¹

The magnetic properties of previously reported hydrothermally as-synthesized $\text{SrFe}_{12}\text{O}_{19}$ platelets show values ranging from negligible coercivity and remanent magnetization,^{21, 42} to values similar to ours for the as-prepared powders.^{21, 36} Higher remanent magnetization values than ours are reported by other groups like Lee J.H. *et al.* for their autoclave synthesis ($48 \text{ Am}^2 \text{ Kg}^{-1}$). Their obtained higher magnetization is due to the formation of larger crystallites, of several micrometers along *ab*-axis.

Hydrothermally synthesized and subsequent calcined $\text{SrFe}_{12}\text{O}_{19}$ samples attain similar saturation magnetization as our samples, with values of $76 \text{ Am}^2 \text{ kg}^{-1}$,³⁶ and $65 \text{ Am}^2 \text{ kg}^{-1}$.⁴² However, the remanent magnetization values ($35 \text{ Am}^2 \text{ kg}^{-1}$ and $\sim 37 \text{ Am}^2 \text{ kg}^{-1}$) are much lower, with a M_r/M_s ratio of about 0.5 as expected for unaligned platelets. The high M_r of our samples is due to the high alignment of the nanoplatelets achieved by SPS. This high alignment is of key importance in order to achieve high energy products.¹¹ On the other hand, the reported coercive field values cover a very wide range, from around

100 kA m⁻¹ to 444.5 kA m⁻¹.^{36, 41-43} The differences in coercive fields are due to different heating rates, calcination temperatures and times, yielding different crystallite sizes and microstructures. It is hard to rationalize the different reported coercivities, as the literature suffers from a general lack of detailed structural characterization. A low coercivity value may be due to insufficient or excessive crystallite growth. It seems, however, that calcination processes often lead to very large crystallites, exceeding the critical size value for single magnetic domain systems. The small size of the crystallites synthesized in the present study, and more specifically the small thickness of the starting nanoplatelets is the main strength of the method reported here, resulting in a larger margin for crystallite growth to occur before domain wall formation starts. Compaction of nanoplatelets through SPS entails fast densification with minor crystallite growth, accompanied by an induced alignment of the magnetic platelets.

Conclusions

SrFe₁₂O₁₉ hexagonal nanoplatelets have been synthesized by the supercritical hydrothermal flow method. The combined analysis of Rietveld refinement of X-ray diffraction data, TEM, and AFM demonstrates that purity, particle size and diameter/thickness ratio of the nanoplatelets can be tuned by varying the Fe/Sr ratio in the precursor solution.

Spark Plasma Sintering of the hydrothermally synthesized powders leads to bulk magnets with highly orientated nanocrystallites without the need for an externally applied magnetic field. This high degree of alignment is a consequence of the platelet-like morphology of the initial nanoparticles. This gives rise to single-crystal-like properties, which could also be of interest in other systems where physical properties have a high directional dependency, like piezoelectric effects, thermoelectric materials and superconductors. All samples exhibit crystallite growth during SPS compaction, especially along the direction of magnetization (the *c*-axis), enhancing the magnetic properties without reaching excessively large sizes, *i.e.*, above the multi-domain region.

A direct relationship between the magnetic and structural properties is drawn for all samples. Controlling the nanostructure throughout the process allows tailoring of the magnetic properties in the final product. The highest resulting maximum energy product is $BH_{\max} = 26 \text{ kJ m}^{-3}$, starting from $BH_{\max} = 0.84 \text{ kJ m}^{-3}$ in the as-synthesized powder.

Acknowledgements

This work was supported by the Danish Research Council for Technology and Production Sciences through a Sapere Aude grant (Improved Permanent Magnets through Nanostructuring), the Danish National Research Foundation (Center for Materials Crystallography DNRF93), and from the Danish Research Council for Nature and Universe (Danscatt). We gratefully acknowledge beamtime granted by SPring8 to perform the high-resolution powder diffraction data collection.

Supporting Information

Supporting Information is available from the Wiley Online Library or from the author.

References

1. I. Matsui, *Jpn J Appl Phys* 1, 2006, **45**, 8302-8307.
2. D. K. Jang and J. H. Chang, *Microsyst Technol*, 2013, **19**, 1601-1606.
3. M. A. Riley, A. D. Walmsley and I. R. Harris, *J Prosthet Dent*, 2001, **86**, 137-142.
4. N. R. Routley and K. J. Carlton, *Magn Reson Imaging*, 2004, **22**, 1145-1151.
5. S. Tammaruckwattana and K. Ohyama, presented in part at the IEEE Ind. Elec., Vienna, 2013.
6. R. L. Moss, E. Tzimas, H. Kara, P. Willis and J. Kooroshy, *Critical Metals in Strategic Energy Technologies*, European Union, Luxembourg: Publications Office of the European Union, 2011.
7. M. Humphries, *Rare Earth Elements: The Global Supply Chain*, Congressional Research Service, 2011.
8. G. C. Hadjipanayis, *J Magn Magn Mater*, 1999, **200**, 373-391.
9. E. F. Kneller and R. Hawig, *IEEE Trans Magn*, 1991, **27**, 3588-3600.
10. R. C. Pullar, *Prog Mater Sci*, 2012, **57**, 1191-1334.
11. J. M. D. Coey, *IEEE Trans Magn*, 2011, **47**, 4671-4681.
12. M. Jurczyk, J. S. Cook and S. J. Collocott, *J Alloys Compd*, 1995, **217**, 65-68.
13. S. V. Ketov, Y. D. Yagodkin, A. L. Lebed, Y. V. Chernopyatova and K. Khlopkov, *J Magn Magn Mater*, 2006, **300**, E479-E481.
14. E. Wu, S. J. Campbell and W. A. Kaczmarek, *J Magn Magn Mater*, 1998, **177**, 255-256.
15. W. A. Kaczmarek, B. Idzikowski and K. H. Muller, *J Magn Magn Mater*, 1998, **177**, 921-922.
16. M. Stingaciu, T. M., McGuinness and M. Christensen, *Scientific Reports*, 2015, **5**, 14112.
17. Y. Hakuta, T. Adschiri, T. Suzuki, T. Chida, K. Seino and K. Arai, *J Am Ceram Soc*, 1998, **81**, 2461-2464.
18. B. S. Bhoelan, C. H. Stevering, A. T. J. van der Boog and M. A. G. van der Heyden, *Clin Toxicol*, 2014, **52**, 584-593.
19. A. L. Xia, C. H. Zuo, L. Chen, C. G. Jin and Y. H. Lv, *J Magn Magn Mater*, 2013, **332**, 186-191.
20. A. L. Xia, X. Z. Hu, D. K. Li, L. Chen, C. G. Jin, C. H. Zuo and S. B. Su, *Electron Mater Lett*, 2014, **10**, 423-426.
21. D. Primc, M. Drogenik and D. Makovec, *Eur J Inorg Chem*, 2011, DOI: DOI 10.1002/ejic.201100326, 3802-3809.
22. A. Hilczer, B. Andrzejewski, E. Markiewicz, K. Kowalska and A. Pietraszko, *Phase Transitions*, 2014, **87**, 938-952.
23. J. H. Lee, T. B. Byeon, H. J. Lee, C. G. Kim and T. O. Kim, *J Phys IV*, 1997, **7**, 751-752.
24. J. L. Mi, S. Johnsen, C. Clausen, P. Hald, N. Lock, L. So and B. B. Iversen, *J Mater Res*, 2013, **28**, 333-339.
25. S. Adachi, T. Oguchi, H. Tanida, S. Y. Park, H. Shimizu, H. Miyatake, N. Kamiya, Y. Shiro, Y. Inoue, T. Ueki and T. Iizuka, *Nucl Instrum Methods Phys Res Sect A*, 2001, **467**, 711-714.
26. J. Rodriguez-Carvajal, *Phys B*, 1993, **192**, 55-69.
27. P. Thompson, D. E. Cox and J. B. Hastings, *J Appl Crystallogr*, 1987, **20**, 79-83.
28. E. Jansen, A. Kyek, W. Schafer and U. Schwertmann, *Appl Phys A Mater Sci Process*, 2002, **74**, S1004-S1006.
29. K. Momma and F. Izumi, *J Appl Crystallogr*, 2011, **44**, 1272-1276.
30. E. C. Stoner and E. P. Wohlfarth, *Philos Trans R Soc A*, 1948, **240**, 599-642.
31. W. A. Dollase, *J Appl Crystallogr*, 1986, **19**, 267-272.
32. F. Bachmann, R. Hielscher and H. Schaeben, *Solid State Phenom*, 2010, **160**, 63-68.
33. D. Mainprice, R. Hielscher and H. Schaeben, *Geol Soc Spec Pub*, 2011, **360**, 175-192.
34. Z. F. Zi, Y. P. Sun, X. B. Zhu, Z. R. Yang, J. M. Dai and W. H. Song, *J Magn Magn Mater*, 2008, **320**, 2746-2751.

35. H. Luo, B. K. Rai, S. R. Mishra, V. V. Nguyen and J. P. Liu, *J Magn Magn Mater*, 2012, **324**, 2602-2608.
36. M. Jean, V. Nachbaur, J. Bran and J. M. Le Breton, *J Alloys Compd*, 2010, **496**, 306-312.
37. D. Y. Chen, Y. Y. Meng, D. C. Zeng, Z. W. Liu, H. Y. Yu and X. C. Zhong, *Mater Lett*, 2012, **76**, 84-86.
38. X. Tang, Y. M. Wang, Z. Luo, L. S. Wang, R. Y. Hong and W. G. Feng, *Prog Org Coat*, 2012, **75**, 124-130.
39. X. Tang, R. Y. Hong, W. G. Feng and D. Badami, *J Alloys Compd*, 2013, **562**, 211-218.
40. A. Das, A. Roychowdhury, S. P. Pati, S. Bandyopadhyay and D. Das, *Phys Scr*, 2015, **90**.
41. A. Ataie and S. Heshmati-Manesh, *J Eur Ceram Soc*, 2001, **21**, 1951-1955.
42. A. Baykal, M. S. Toprak, Z. Durmus and H. Sozeri, *J Supercond Novel Magn*, 2012, **25**, 2081-2085.
43. J. F. Wang, C. B. Ponton, R. Grossinger and I. R. Harris, *J Alloys Compd*, 2004, **369**, 170-177.